On the Origin of the Local Hardening Zone on Welded Stainless Clad Steel Plates

Rami Ghorbel, Ahmed Ktari & Nader Haddar

To cite this article: Rami Ghorbel, Ahmed Ktari & Nader Haddar (2022) On the Origin of the Local Hardening Zone on Welded Stainless Clad Steel Plates, Fusion Science and Technology, 78:6, 503-511, DOI: 10.1080/15361055.2022.2051923

To link to this article: https://doi.org/10.1080/15361055.2022.2051923

On the Origin of the Local Hardening Zone on Welded Stainless Clad Steel Plates

Rami Ghorbel,[a]* Ahmed Ktari,[a,b] and Nader Haddar[a]

[a]*Université de Sfax, Ecole Nationale d'Ingénieurs de Sfax, Laboratoire Génie des Matériaux et Environnement, Sfax, B.P.1173-3038, Tunisia*

[b]*Laboratory of Mechanics, Surface and Materials Processing, MSMP-EA7350, Arts et Métiers ParisTech, 2 cours des Arts et Métiers, 13617, Aix-en-Provence, France*

Received November 25, 2021
Accepted for Publication March 8, 2022

Abstract — *The joining of stainless clad steel plates (SCSPs) by welding processes is relatively difficult due to differences in the chemical compositions and the physical and mechanical properties between both the carbon and the stainless steels comprising the clad material. These welded structures often suffer from several structural integrity problems such as bulging phenomena that can appear after bending tests, in the welded zone, due to the presence of a local hardening zone (LHZ). The main purpose of this paper is to investigate the origin of the LHZ typically produced in the welded joint of SCSPs after the bending operation. Optical micrographs revealed the presence of a typical pearlitic-ferritic structure in the welded zone filled with E7018 metal and a dendritic δ-ferrite structure solidified under a skeletal form in the welded zone filled with ER316L metal. The microstructure of the weld metal transition zone (WMTZ) filled with ER309L metal shows the presence of martensitic laths as well as cellular and columnar structures. In addition, the WMTZ revealed the presence of three types of grain boundaries, which are formed during the gas tungsten arc welding process: solidification sub-grain boundary, solidification grain boundary, and migrated grain boundary. Vickers microhardness measurements performed along the thickness of the welded joint showed that the highest microhardness value (406 HV) was observed at the WMTZ. The significant increase of the microhardness value in this transition zone was attributed to the presence of martensitic laths as well as cellular and columnar structures.*

Keywords — *Austenitic stainless clad material, SMAW process, GTAW process, microstructure, local hardening zone.*

Note — *Some figures may be in color only in the electronic version.*

I. INTRODUCTION

Since stainless steels are expensive, many efforts have been devoted to develop stainless clad steel plates[1–3] (SCSPs). These SCSPs are likely to be economical solutions for building pressure vessels, storage tanks, and heat exchangers.[4] In fact, these bi-materials present interesting properties such as excellent corrosion resistance, good environmental stability, high specific resistance, and reduced production cost. Therefore, these austenitic stainless clad steel materials are currently used in a wide range of industrial applications (petroleum, petrochemical, shipbuilding, nuclear and pressure vessel industries, etc.).[1,4,5]

Good weldability is one the most important attributes of carbon steel and austenitic stainless steel. For that reason, austenitic stainless clad steel has gained more worldwide applications compared to other clad steels. The welding process is currently the main method used in the industrial field to join and assemble SCSPs (Refs. 1, 2, and 5). However, welding at high temperature requires significant attention when welding SCSPs to avoid precipitation of chrome carbide ($Cr_{23}C_6$) at the welding interfaces leading, consequently, to the presence of a martensitic structure

*E-mail: rami.ghorbel@enis.tn

during the cooling phase.[4] Actually, the parent metal and the clad layer in SCSP materials have substantial differences in physical and mechanical properties, such as heat conductivity and thermal expansion coefficient.[5] The difference in properties may lead to high residual thermal stress formation at the welding-clad interface during the welding and cooling processes.[6,7] In addition, clear variation in chemical composition is often present between the clad layer and the substrate. Alloy elements (i.e., Cr and Ni) in the clad layer can easily dilute and diffuse into a carbon steel welded bead, leading to low contents of alloy elements and low corrosion resistance of the clad layer.[5] Furthermore, excessive diffusion of alloying elements can result in the formation of $Cr_{23}C_6$ carbides, leading to severe intergranular depletion (Cr depletion) and intergranular cracks. For these reasons, it is crucial to overcome the technological difficulties generated by the considerable differences between materials to be joined in terms of structure, atomic bonds, and physico-chemical properties.[8–10]

In addition, several researchers have focused on investigating the relationship between microstructure and mechanical properties.[11–15] Sabzi and Dezfuli[11] have reported that important properties such as hardness, toughness, strength, and flexibility are affected by the microstructure and solidification behavior of the weld metal. In addition to that, Sabzi and Farzam[12] have reported that the carbide formation in the weld zone improves the toughness and strength compared to the base metal in Hadfield steels. Furthermore, Anijdan et al.[13] have reported that fracture analysis of a dissimilar joint (DP600/AISI304) is a complex endeavor due to differences in the physical and mechanical properties of the welded sheets.

In earlier work, Ghorbel et al.[5] studied the evolution of temperature distribution during multipass welding of SCSPs using a combined shielded metal arc welding (SMAW) process/gas tungsten arc welding (GTAW) process and its effect on the studied bi-materials and evaluated the welding reliability. The first results showed the presence of angular distortion and longitudinal shrinkage after welding at 9.1 deg and 8 mm, respectively. Ghorbel et al. reported that these distortions were generated by residual stresses during the welding process. They also revealed that despite the large thickness of the carbon steel side, distortion occurred on the thin stainless steel side. The second part of Ghorbel et al.'s investigation focused on evaluating the integrity of the welded joint. Tensile tests and bent tests were carried out. The tensile tests results indicate that the specimens were fractured at the base metal about 4 cm away from the welded joint. Furthermore, examination of the bent specimens' surfaces revealed the exception of any sign of cracks or tears. However, the results showed the presence of a bulging phenomenon located on the welded joint bent surfaces, which proves the presence of a local hardening zone (LHZ) with low plasticity.

Yet, the previous work was limited to evaluating the welded joint performance using conventional tensile and bend tests. Herein, and because of the presence of the LHZ, the current paper aims to deepen the investigation in order to get a coherent understanding of this phenomenon. In this study, it is well known that the main cause producing the LHZ is the martensite. The purpose of this study then is to specify that the martensite formation was produced either due to the plastic deformation that supervenes during the bend test or due to the presence of a martensitic structure formation during the welding. For this, the microstructure and the microhardness of the welded joint were studied.

II. MATERIALS AND METHODS

Two plates with dimensions of 200 × 400 mm were extracted from a SCSP obtained by hot-roll bonding of a 12-mm low carbon steel (ASTM A283 Grade C) and a 3-mm austenitic stainless steel clad layer (ASTM A240 TP316L). The geometrical and the dimensional details of the test coupon plates are given in Fig. 1. The chemical composition and the monotonic mechanical properties of the SCSP base material studied in this work are given in Tables I and II, respectively.

In this study, the welding process was carried out using three filler metals—E7018, ER316L, and ER309L—to join the low carbon steel (ASTM A283

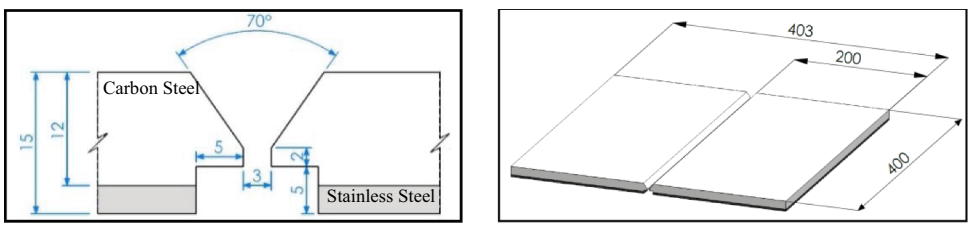

Fig. 1. (a) Fitting up operation form and dimensional details of the U-V shape[5] and (b) dimensional details of the test coupon plates.

TABLE I

Chemical Composition of the SCSPs and the Filler Metals*

	Elements	Carbon	Silicon	Manganese	Phosphorus	Sulfur	Chromium	Nickel	Molybdenum
Base material	A283 Grade C	0.167	0.172	0.479	0.019	0.022	—	—	—
	A240 TP316L	0.017	0.514	1.124	0.038	0.002	16.654	10.109	2.092
Filler metals	ER316L	0.08	0.53	1.17	0.053	0.008	16.18	10.55	1.90
	E7018	0.23	0.171	0.402	0.032	0.012	0.024	0.021	<0.002
	ER309L	0.025	0.45	1.8	0.02	0.02	24	13	—

*In units of weight percent. Reference 5.

TABLE II

Mechanical Properties of the SCSPs (A283 Grade C + A240 TP316L) at Room Temperature

Tensile strength	*Rm* (MPa)	438
Yield strength	*Re* (MPa)	418
Young's modulus	*E* (GPa)	210
Poisson's ratio	υ	0.3
Elongation	*A* (%)	30

Grade C), the austenitic stainless steel (ASTM A240 TP316L), and the transition zone, respectively. Typical chemical compositions of these filler metals are given in Table I. Nine passes were performed as follows: Three passes on the carbon steel side were performed using the SMAW process, and two passes in the transition phase and four passes on the stainless steel side were performed using the GTAW process. Figure 2 is a schematic view of the welding bead layers on the austenitic stainless cladded steel. The used filler metal for each pass and its corresponding welding parameters are given in Table III.

Since GTAW and SMAW are basically manual processes, a qualified welder was selected to perform the welding process. Welding was carried out in an uphill position. Filler metals were consumed during the welding operation. Consequently, replacement of the consumed electrode was required. The welding region was cleaned of slags and impurities after every filler metal replacement to obtain a homogeneous defect-free welded bead. The first-pass weld bead was carried out using a 2.5-mm-diameter electrode on the carbon steel side. Grinding operation for weld recovery was conducted during this pass. On the same steel side, the filling and covering (i.e., last pass on the carbon steel side) passes were carried out using 3.2-mm-diameter electrode. Filling and covering passes were performed using a 2.4-mm-diameter electrode on the stainless steel side. After each pass, a cooling time was allowed until the highest temperature in the welded joint reached 150°C (inter-pass temperature). This inter-pass temperature was controlled using a Fluke®566 infrared thermometer. During each pass, the current *I* and voltage *U* were measured during the welding process using a voltmeter and an ammeter linked to the weld circuit. For each pass the welding speed *v* was calculated using the following relationship [Eq. (1)]:

$$v = \mathit{average}(\mathit{welded\ distances}/\mathit{times}). \quad (1)$$

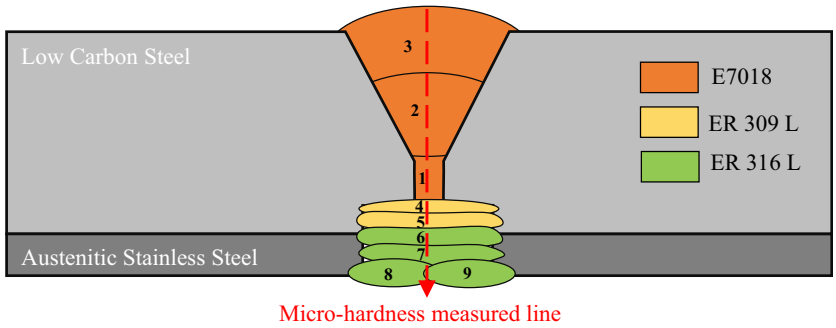

Fig. 2. Schematic view of different passes of the stainless clad steel welding process.[5]

TABLE III

Welding Parameters Used in the SCSP Multipass Welding Process*

Weld Pass Number	Filler Metal	Filler Metal Diameter (mm)	Current and Polarity	Welding Current (A)	Arc Voltage (V)	Welding Speed (mm/s)	Heat Input (kJ/mm)
1	E7018	2.5	DC+[a]	85	22	1.43	1.31
2	E7018	3.2	DC+	116	22	1.13	2.27
3	E7018	3.2	DC+	113	24	1.86	1.46
4	ER309L	2.4	DC-[b]	133	10	1.3	1.02
5	ER309L	2.4	DC-	141	11	1.18	1.31
6	ER316L	2.4	DC-	142	11	1.1	1.42
7	ER316L	2.4	DC-	140	11	0.93	1.66
8	ER316L	2.4	DC-	130	10	1.25	1.04
9	ER316L	2.4	DC-	133	10	0.86	1.55

*Reference 5.
[a]DC+: direct-current reverse polarity.
[b]DC-: direct-current straight polarity.

All these parameters are used to calculate the heat input using the following formula [Eq. (2)]:

$$HI = (U \times I \times 60/1000 \times v). \quad (2)$$

The welding parameters for each pass are given in Table III. For more details concerning the welding process, see Ref. 5.

A specimen with dimensions of 120 × 15 × 9.5 mm was extracted from the welded test coupon and then was used to perform the micrographic and the microhardness examinations. Both sides of the specimen were mechanically polished using SiC grit paper with a grit number varying from 280 to 1200, followed by a final polishing using 6-, 3-, and 1-µm diamond pastes, respectively. The first side was used to carry out the microstructure examination. For this, the carbon steel was chemically etched using 3% of a nitric acid alcohol solution for 5 s while the austenitic stainless steel was electrolytically etched using 10% of an oxalic acid solution in distilled water at 6 V for 20s. The microstructure of the welded joint was investigated using a LEICA® metallographic microscope. Given the expected complexity of the microstructure in the welded joint, since it presents the assembly of a bi-material with three different filler metals, the second side was used to perform the microhardness measurement from the top to the bottom of the weld zone, as depicted in Fig. 2. The microhardness tests were conducted with an Innova® testing machine, using a Vickers indenter under a load of 0.1 kg.

III. RESULTS AND DISCUSSION

In this paper, a microstructural investigation of the welded joint is carried out in order to determine the different phases presented in the welded joint and to

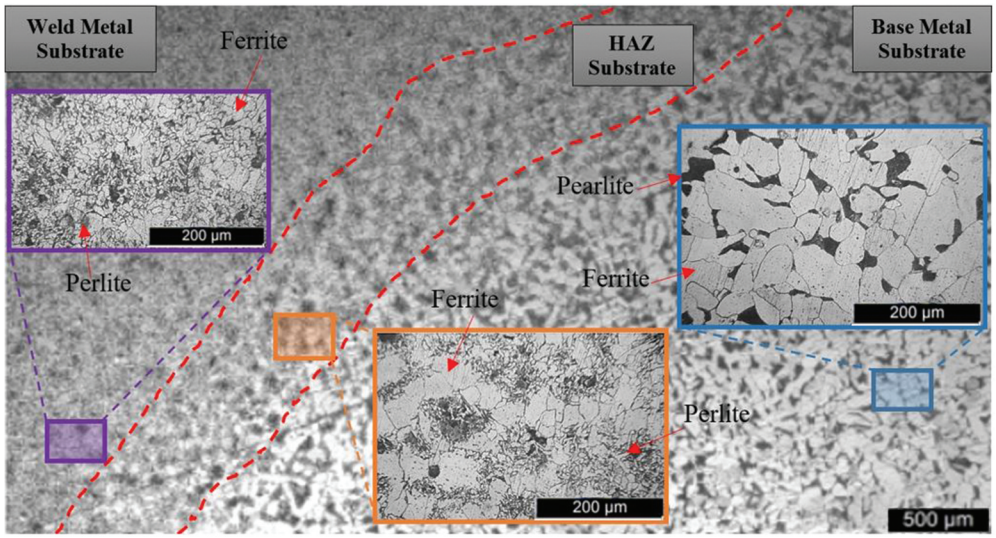

Fig. 3. Metallographic examination details of the welded joint filled with E7018.

study, consequently, whether they contain the martensite. The microstructure evolution across the welded joint filled with E7018 is shown in Fig. 3. The base metal substrate is composed of perlite (dark grains) and ferrite (right grains) phases. The pearlitic grains became finer while going from the base metal substrate zone to the weld metal substrate zone passing through the heat affected zone (HAZ) substrate.

The microstructure of the welded joint zone filled with ER316L is shown in Fig. 4. The examination of the base metal clad layer revealed the presence of a largely austenitic (γ-white) structure with the presence of some twins. Far away from the fusion line, the microstructure of the weld metal clad layer presents an austenite matrix and a dendritic δ-ferrite, which mainly solidified in skeletal morphologies.

The microstructure of the welded joint zone filled with ER309L was also evaluated. Figure 5 shows that the microstructure of the weld metal is mainly austenitic-ferritic, and it reveals the presence of elongated columnar and cellular structures as well as stable

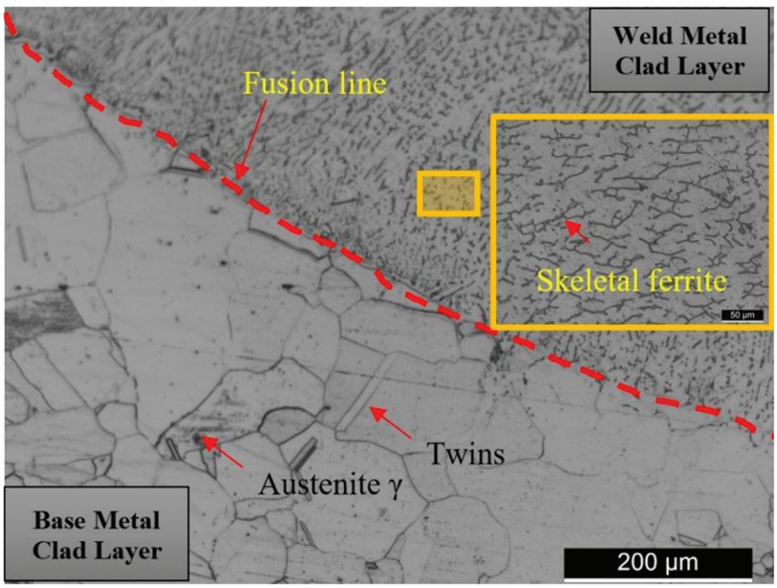

Fig. 4. Metallographic examination details of the welded joint filled with ER316L.

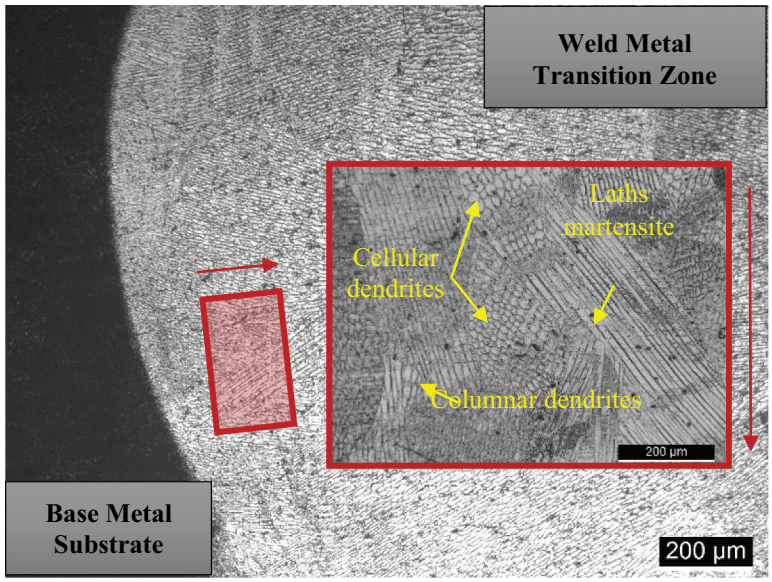

Fig. 5. Metallographic examination details of the welded joint filled with ER-309L.

martensitic laths. In addition, it is obvious that the weld metal in the welded joint solidifies according to the austenitic-ferritic solidification mode. Similar findings were reported by Tabrizi et al.[16] and Sabzi et al.[17] when they studied the effect of pulsed and continuous current using the GTAW process during the welding of Type 316L stainless steel as well as the influence of pulsed current change using the GTAW process on the microstructure evolution of the dissimilar welded joint (Type 316L stainless steel/Type 310S stainless steel), respectively. The presence of cellular and columnar dendrites proves a high solidification rate, which depends on the G/R ratio, where G is the thermal gradient and R is the growth rate.[18] Indeed, during the welding, there is a difference of solidification time between the liquid L and the solid S interface (an improper solvent mixture). This patterns a difference in composition, which leads to constitutional supercooling. When the weld metal transition phase solidifies under the liquidus temperature, a transformation from a planar to a cellular or dendritic mode of solidification will occur. This depends on the temperature range of the freezing ΔT and the growth rate R. When the G/R ratio is less than that of $\Delta T/DL$, the cellular and the columnar dendritic type of solidification occurs; DL represents the diffusion of the solute coefficient in the liquid. Figure 6 presents the effect of the temperature gradient G and the growth rate R on the morphology and size of the microstructure solidification.[19] It is to be noted that the cellular and columnar structures are characterized by their martensitic nature as already reported by Rathod et al.[20]

Literally, defects generated by the welding process such as alloying element segregation, inclusions, and solidification cracks as well as all the properties of the welded joint are related to such a grain boundary character. In this study, analysis of the weld metal transition zone (WMTZ) revealed three types of grain boundaries, which are formed during the GTAW process: solidification sub-grain boundary (SSGB), solidification grain boundary (SGB), and migrated grain boundary (MGB) (Fig. 7). Tabrizi et al.[16] have reported in their work that compared with the original grain boundaries, SSGBs usually have different orientations and chemical compositions. Sabzi et al.[17] have reported that the MGB reduces the newly formed grain boundary energy. However, the SGB, which develops during weld pool solidification and along its trailing edge, is the immediate result of competitive growth in the WMTZ.

Overall, the carbon steel and the stainless steel metallographic examination exhibited typical microstructures with no sign of a martensitic phase. However, the WMTZ revealed the presence of a martensitic phase under laths, and cellular and columnar morphologies. Hence, in order to confirm these findings, microhardness measurement was conducted, and the measured values were evaluated.

The microhardness profile along the L1 direction is shown in Fig. 8. It is clear that both the weld metal clad

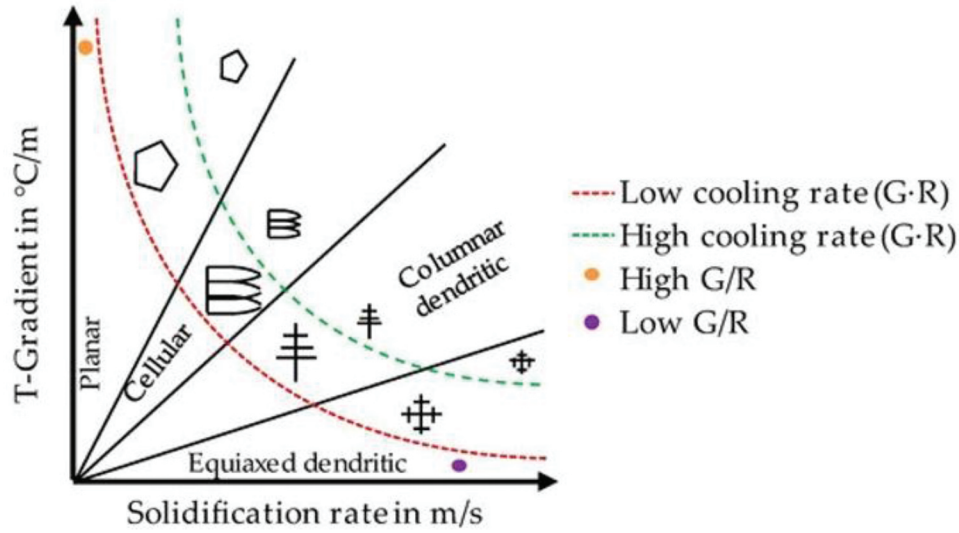

Fig. 6. Effect of temperature gradient G and growth rate R on the morphology and size of microstructure solidification.[19]

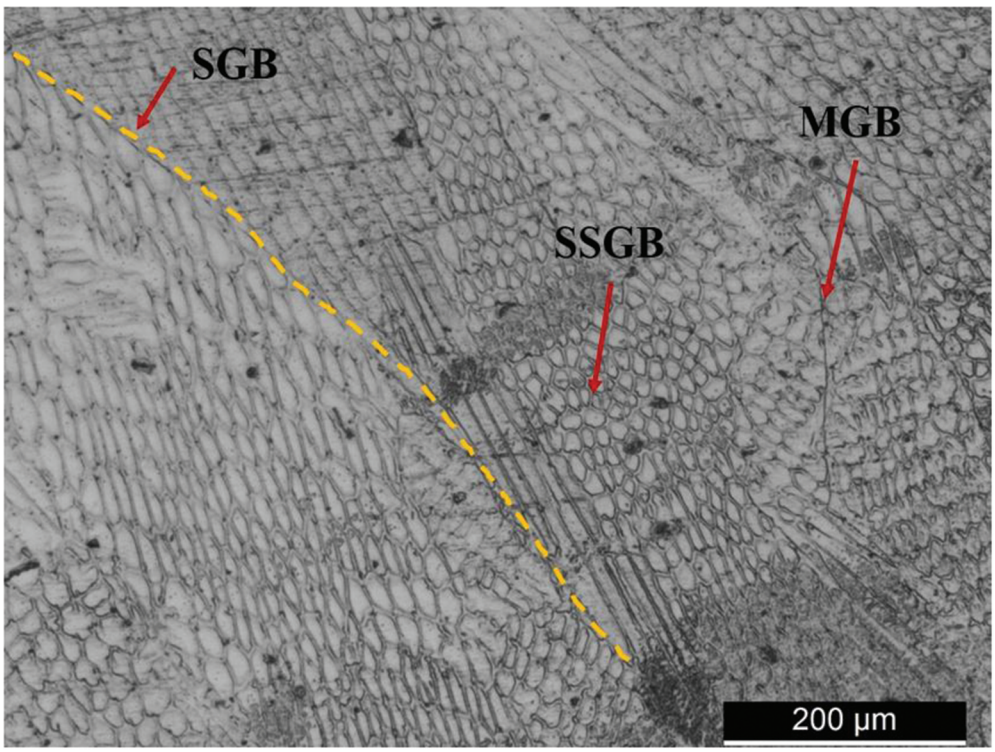

Fig. 7. Optical micrograph of the grain boundaries formed in the WMTZ.

layer (average 221 ± 19 HV) and the weld metal substrate (average 213 ± 5 HV) have shown no large variation in microhardness values. In contrast, the microhardness value of the WMTZ increased significantly and reached about 406 HV. This is can be attributed to the presence of the martensitic phase previously observed in Fig. 5 as well as the presence of the cellular and columnar dendritic structures.

On the basis of the previous discussion, the main cause that produces the LHZ is the presence of a martensitic structure, which was observed

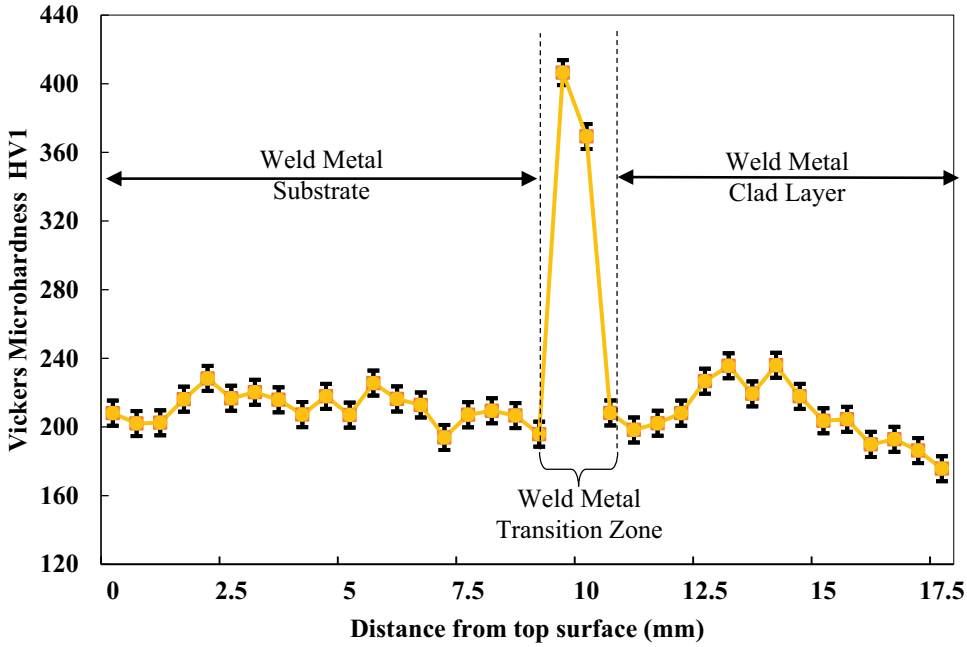

Fig. 8. Microhardness of the welded joint along the weld thickness.

microscopically and confirmed by the microhardness measurements.

IV. CONCLUSIONS

In this paper, the origin of the LHZ found on the welded SCSPs was investigated. From this research, the following main conclusions can be drawn:

1. In terms of metallographic examination, the microstructure of the welded joint filled with E7018 explicitly consists of perlite and ferrite structure. The observed microstructure shows no sign of a martensitic phase. Moreover, the microstructure of the welded joint filled with ER316L mainly reveals an austenitic matrix in the base metal clad layer with the presence of some twins. However, the weld metal clad layer microstructure shows the presence of a dendritic δ-ferrite that is solidified under a skeletal morphology. The micrographic observations reveal the exemption of the martensitic phase. Furthermore, the microstructure of the welded joint filled with ER309L indicates the presence of martensitic laths as well as cellular and columnar structures in the WMTZ.
2. Vickers microhardness measurements performed along the thickness of the welded joint showed that the highest value of the microhardness was measured at the WMTZ of the welded joint (406 HV). The significant increase in the microhardness value was attributed to the presence of martensitic laths as well as the cellular and columnar structures.

In view of the outcomes obtained, it can be asserted that the main cause producing the LHZ is the martensitic structure observed in the WMTZ. In order to avoid the formation of martensitic zones in the welded joint, efforts are ongoing to study the effect of heat input on the dilution rate and subsequently on the nature of the presented phases.

Acknowledgments

The authors would like to thank M. T. Hbaieb and A. Badri, of SOCOMENIN Company, for their knowledgeable help and support.

Disclosure Statement

No potential conflict of interest was reported by the authors.

ORCID

Rami Ghorbel http://orcid.org/0000-0003-2957-9258
Ahmed Ktari http://orcid.org/0000-0002-2731-0717

References

1. Z. DHIB et al., "Cladding of Low-Carbon Steel to Austenitic Stainless Steel by Hot-Roll Bonding: Microstructure and Mechanical Properties Before and After Welding," *Mater. Sci. Eng.*, **656**, 130 (2016); https://doi.org/10.1016/j.msea.2015.12.088.
2. R. N. VENKATESWARA et al., "Weld Overlay Cladding of High Strength Low Alloy Steel with Austenitic Stainless Steel—Structure and Properties," *Mater. Des.*, **32**, *4*, 2496 (2011); https://doi.org/10.1016/j.matdes.2010.10.026.
3. B. X. LIU et al., "The Tensile Behaviors and Fracture Characteristics of Stainless Steel Clad Plates with Different Interfacial Status," *Mater. Sci. Eng.*, **679**, 172 (2017); https://doi.org/10.1016/j.msea.2016.10.033.
4. Q. AN et al., "Microstructure and Mechanical Properties of Stainless-Steel Clad Plate Joints Produced by TIG and MAG Hybrid Welding," *J. Adhes. Sci. Technol.*, **34**, *6*, 670 (2020); https://doi.org/10.1080/01694243.2019.1677087.
5. R. GHORBEL et al., "Experimental Analysis of Temperature Field and Distortions in Multi-Pass Welding of Stainless Cladded Steel," *Int. J. Adv. Manuf. Technol.*, **113**, 3525 (2021); https://doi.org/10.1007/s00170-021-06788-y.
6. L. LI et al., "Welding L415/316L Bimetal Composite Pipe Using Post-Internal-Welding Process," *Trans. Indian Inst. Met.*, **73**, 675 (2020); https://doi.org/10.1007/s12666-020-01868-1.
7. W. WANG et al., "Microstructure and Corrosion Resistance of Butt Joint of 1Cr18Ni9Ti+ Q235 Composite Plate," *Trans. China Weld. Inst.*, **6** (2010).
8. D. O. BOKOV et al., "Effect of Pin Shape on Thermal History of Aluminum-Steel Friction Stir Welded Joint: Computational Fluid Dynamic Modeling and Validation," *Materials*, **14**, *24*, 7883 (2021); https://doi.org/10.3390/ma14247883.
9. A. SAURAW et al., "Study on Microstructural Characterization, Mechanical Properties and Residual Stress of GTAW Dissimilar Joints of P91 and P22 Steels," *Materials*, **14**, *21*, 6591 (2021); https://doi.org/10.3390/ma14216591.
10. Y. SUN et al., "Mechanical Properties Evaluation and Crack Propagation Behavior in Dissimilar Metal Welded Joints of 304 L Austenitic Stainless Steel and SA508 Low-Alloy Steel," *Sci. Technol. Nucl. Install.*, **2022**, 3038397 (2022); https://doi.org/10.1155/2022/3038397.
11. M. SABZI and S. M. DEZFULI, "Drastic Improvement in Mechanical Properties and Weldability of 316L Stainless Steel Weld Joints by Using Electromagnetic Vibration During GTAW Process," *J. Manuf. Processes*, **33**, 74 (2018); https://doi.org/10.1016/j.jmapro.2018.05.002.
12. M. SABZI and M. FARZAM, "Hadfield Manganese Austenitic Steel: A Review of Manufacturing Processes and Properties," *Mater. Res. Express*, **6**, *10*, 1065c2 (2019); https://doi.org/10.1088/2053-1591/ab3ee3.
13. S. M.ANIJDAN et al., "Optimization of Spot Welding Process Parameters in Dissimilar Joint of Dual Phase Steel DP600 and AISI 304 Stainless Steel to Achieve the Highest Level of Shear-Tensile Strength," *Mater. Sci. Eng.*, **726**, 120 (2018); https://doi.org/10.1016/j.msea.2018.04.072.
14. M. SABZI et al., "Deposition of Ni-Tungsten Carbide Nanocomposite Coating by TIG Welding: Characterization and Control of Microstructure and Wear/Corrosion Responses," *Ceram. Int.*, **44**, *18*, 22816 (2018); https://doi.org/10.1016/j.ceramint.2018.09.073.
15. H. R. JAFARIAN et al., "The Influence of Austenitization Temperature on Microstructural Developments, Mechanical Properties, Fracture Mode and Wear Mechanism of Hadfield High Manganese Steel," *J. Mater. Res. Technol.*, **10**, 819 (2021); https://doi.org/10.1016/j.jmrt.2020.12.003.
16. T. R. TABRIZI et al., "Comparing the Effect of Continuous and Pulsed Current in the GTAW Process of AISI 316L Stainless Steel Welded Joint: Microstructural Evolution, Phase Equilibrium, Mechanical Properties and Fracture Mode," *J. Mater. Res. Technol.*, **15**, 199 (2021); https://doi.org/10.1016/j.jmrt.2021.07.154.
17. M. SABZI et al., "The Effect of Pulse Current Changes in PCGTAW on Microstructural Evolution, Drastic Improvement in Mechanical Properties, and Fracture Mode of Dissimilar Welded Joint of AISI 316L-AISI 310S Stainless Steels," *Mater. Sci. Eng.*, **823**, 141700 (2021); https://doi.org/10.1016/j.msea.2021.141700.
18. E. N. ABBAS et al., "Dissimilar Welding of AISI 309 Stainless Steel to AISI 1020 Carbon Steel Using Arc Stud Welding," *Proc. 1st Int. Conf. Advanced Science and Engineering (ICOASE 2018)*, Duhok, Kurdistan Region, Iraq, October 9–11, 2018, p. 462, IEEE (2018).
19. S. KOU, *Welding Metallurgy*, pp. 431–446, John Wiley & Sons, Hoboken, New Jersey (2003).
20. D. W. RATHOD et al., "Diffusion Control and Metallurgical Behavior of Successive Buttering on Sa508 Steel Using Ni–Fe Alloy and Inconel 182," *Metallogr. Microstruct. Anal.*, **5**, 450 (2016); https://doi.org/10.1007/s13632-016-0311-z.